

Attention-based Shape-Deformation Networks for Artifact-Free Geometry Reconstruction of Lumbar Spine from MR Images

Linchen Qian, Jiasong Chen, Linhai Ma, Timur Urakov, Weiyong Gu, Liang Liang

arXiv:2404.00231v2 [cs.CV] 16 Apr 2024

Abstract—Lumbar disc degeneration, a progressive structural wear and tear of lumbar intervertebral disc, is regarded as an essential role on low back pain, a significant global health concern. Automated lumbar spine geometry reconstruction from MR images will enable fast measurement of medical parameters to evaluate the lumbar status, in order to determine a suitable treatment. Existing image segmentation-based techniques often generate erroneous segments or unstructured point clouds, unsuitable for medical parameter measurement. In this work, we present *TransDeformer*: a novel attention-based deep learning approach that reconstructs the geometry of the lumbar spine with high spatial accuracy and mesh correspondence across patients, and we also present a variant of *TransDeformer* for error estimation. Specially, we devise new attention modules with a new attention formula, which integrate image features and tokenized contour features to predict the displacements of the points on a shape template without the need for image segmentation. The deformed template reveals the lumbar spine geometry in an image. Experiment results show that our *TransDeformer* generates artifact-free geometry outputs, and its variant predicts the error of a reconstructed geometry. Our code is available at <https://github.com/linchenq/TransDeformer-Mesh>.

Index Terms—deep learning, geometry reconstruction, lumbar spine, mesh correspondence, attention

I. INTRODUCTION

GEOMETRY reconstruction of the anatomical structures from medical images helps to improve clinical outcomes such as disease diagnosis accuracy, surgical planning accuracy, and treatment efficacy [1], [2]. Low back pain is a prevalent global health issue associated with activity limitation and absenteeism from work [3], [4], and lumbar disc degeneration, which is the gradual deterioration of the lumbar intervertebral disc, plays a significant role in the onset of this issue [5]. Magnetic Resonance Imaging (MRI) is instrumental in identifying morphological changes and revealing the internal structure of

Linchen Qian, Jiasong Chen, Linhai Ma, and Liang Liang are with the Department of Computer Science, College of Arts and Sciences, University of Miami, Coral Gables, FL 33146, USA (e-mail: linchen.qian@miami.edu; jiasong.chen@miami.edu; l.ma@miami.edu; liang@cs.miami.edu).

Timur Urakov is with the Department of Neurological Surgery, University of Miami Miller School of Medicine, Miami, FL 33136, USA (e-mail: turakov@med.miami.edu).

Weiyong Gu is with the Department of Mechanical and Aerospace Engineering, College of Engineering, University of Miami, Coral Gables, FL 33146, USA (e-mail: wgu@miami.edu).

tissues, which is recognized as a key method for investigating disc degeneration [6]. Consequently, it is essential to model lumbar spine morphology and conduct a quantitative analysis of degeneration cascade using a precise geometric representation [7] that is reconstructed from lumbar spine MR images. Due to individual variations, manual geometry annotation is laborious, and therefore automated image analysis methods are desired for clinical applications.

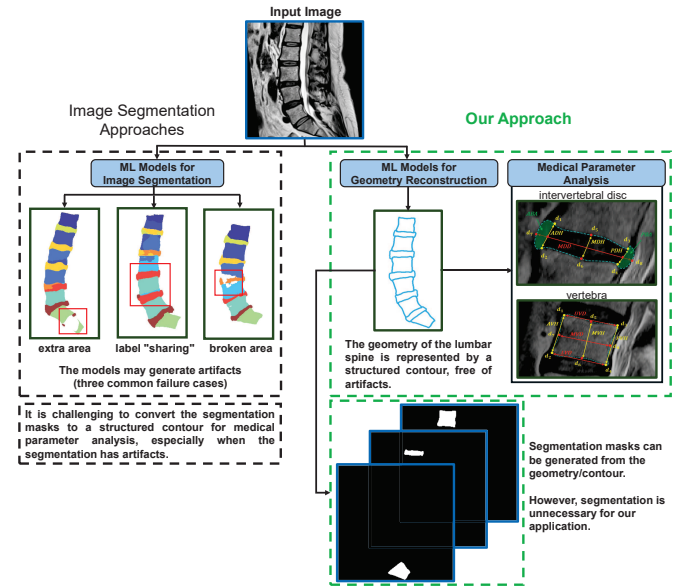


Fig. 1. Comparison of our geometry reconstruction approach (right) and the existing image segmentation approaches (left) for lumbar spine MR image analysis.

Currently, most of the lumbar spine image analysis applications focus on image segmentation and classification [8]. The object masks from image segmentation are not directly usable for measuring many medical parameters related to lumbar disc degeneration in our application, and those masks have to be converted to a mesh, on which the medical parameters could be defined and measured. The mask-to-mesh conversion can be error-prone because segmentation artifacts are often present in the segmentation masks, as illustrated in Fig. 1.

In contrast to segmentation masks, a mesh (i.e., a structured contour) of the lumbar spine is a more precise representation that depicts the anatomy with nodes/points and elements (i.e.,

point connectives), as shown in Fig. 1. This mesh representation facilitates the computation of the medical parameters that reflect disc degeneration status [7], [9]. Moreover, if meshes with the same topology are used for all patients, mesh correspondence across patients will be established, thus supporting consistent geometric analysis using the same reference anatomical structure [10]. Despite the advantages over segmentation masks, automated geometry reconstruction of the lumbar spine with a mesh representation remains a challenge because of anatomical complexity and variations.

In this study, we propose two new deep neural networks, named **UNet-DeformSA** and **TransDeformer**, to reconstruct lumbar spine geometries from 2D sagittal MR images by deforming a mesh template, thereby enabling consistent definition and measurement of the medical parameters related to lumbar disc degeneration. By using new attention modules with a new attention formula, the geometry outputs of our networks are artifact-free. In addition, we propose a third network to estimate the errors of the geometries reconstructed by a network, which facilitates quality control for clinical use.

Due to the 10-page limit, we keep the following sections to be as concise as possible. We can expand the reference list if the reviewers consider it necessary.

II. RELATED WORKS

In our application, the geometry of a lumbar spine is represented by a 2D mesh (see Fig. 1), i.e., a structured contour of the 11 lumbar spine objects including 6 vertebrae and 5 intervertebral discs. Throughout this paper, lumbar spine geometry, shape, and contour are used interchangeably.

As briefly mentioned in the introduction section, in ideal scenarios, the object masks from an image segmentation model could serve as an intermediate representation, from which a mesh could be extracted. In a recent study [11], we evaluated fifteen image segmentation models for our application, (e.g., UNet++ [12], TransUnet [13], Swin-Unet [14], BianqueNet [15]). Although some of these image segmentation models perform well with Dice scores > 0.9 on average, segmentation artifacts are often present in the segmentation masks, which may be (1) extra areas not belonging to any discs or vertebrae, (2) the same class label assigned to two different discs, and (3) broken areas of a disc or vertebrae. A mesh extracted from the segmentation masks with artifacts has the same artifacts and therefore is useless. Thus, the segmentation-and-meshing approach do not work for our application.

A template deformation based approach for geometry reconstruction is a better choice for our application, because it ensures mesh correspondence across patients and thereby enables consistent definitions of medical parameters on a reference anatomical structure (i.e., the template). This type of approaches [16] can be traced back to a method known as active appearance model (AAM) [17] that deforms a shape template with the guidance of the statistical model of object geometry and appearance. It is known that the AAM method will not work if images have complex textures and weak edges. To handle complex data, in the pre-deep learning era, classic machine learning (ML) methods were used for

template initialization and nonrigid deformation. For example, in the application of heart geometry modeling from CT images [18], a template was initialized by an object detector and then deformed by using an object boundary detector [18], where the detectors were built on probabilistic boosting-tree techniques. In the application of aortic valve leaflet geometry modeling from CT images [19], a template was deformed by using linear coding with a dictionary of representative shapes. Deep learning (DL) has significantly changed the landscape of medical image analysis [2]. In the next few paragraphs, we provide a brief review of the existing medical DL approaches for geometry reconstruction with template deformation.

Graph convolution network (GCN) has demonstrated ground-breaking performance in geometry modeling by leveraging the structural relationships among vertices and edges [20]. GCNs can predict displacements of points/vertices of a template using image features. Wickramasinghe et al. proposed Voxel2Mesh, a GCN-based model with adaptive sampling and pooling strategies for geometry reconstruction of liver, hippocampus and synaptic junction [21]. Although this Voxel2Mesh approach outperformed several segmentation-based methods, it generated an uncertain number of vertices, thus lacking mesh correspondence across patients. Kong et al. proposed a compound framework fusing a UNet with GCN to deform templates for whole-heart geometry reconstruction on cardiac datasets [22]. As will be shown in our experiments, such a UNet-GCN approach still generates geometry artifacts in our application.

Instead of treating a geometry as a graph, some studies regards geometry reconstruction as a template-image registration task, wherein a diffeomorphic displacement field [23] is generated by a network to transform an initial template mesh to the target. For example, Pak et al. proposed DeepCarve that predicted a regular-grid displacement field by a UNet and used it to deform a pre-defined template of left-ventricle and aorta complex on a dataset of 80 cardiac CT scans [24]. As will be shown in our experiments, such a UNet-Disp approach is very sensitive to template initialization, such that some perturbation on initial position of the template may aggravate the quality of the output geometry.

Recently, Transformers utilizing an attention mechanism, have been adopted for image classification and segmentation [25]. The output of a scaled dot-product attention in Transformers is mathematically formulated as:

$$Out(Q, K, V) = \text{softmax} \left(\frac{QK^T}{\sqrt{d_k}} \right) V \quad (1)$$

Linear projections are applied to the input vectors, resulting in query (Q), key (K), and value (V) matrices. d_k is the dimension of a query or key. Unlike convolution which is akin to uniform filtering across different locations on the input, the attention mechanism in Transformers operates as an adaptive filter, where its weights are determined by interrelations between each paired tokens.

In this paper, we present the first study on exploring the potential of attention mechanisms for geometry reconstruction of lumbar spine from MR images using a template.

III. METHODS

As illustrated by Fig. 1, the goal of our application is to reconstruct lumbar spine geometries from 2D sagittal MR images and then measure the medical parameters that are often used for lumbar disc degeneration assessment. For this purpose, the geometry of a lumbar spine is represented by a 2D mesh, i.e., a structured contour of the 11 lumbar spine components including 6 vertebrae and 5 intervertebral discs.

We designed two novel networks for lumbar spine geometry reconstruction, named **UNet-DeformSA** and **TransDeformer**. The UNet-DeformSA model (Fig. 2) has a UNet backbone and a shape self-attention (SSA) mechanism that sets it apart from the existing models. The TransDeformer model (Fig. 3) gets rid of the UNet backbone by using cross-attention between shape and image as well as shape self-attention and image self-attention, which further improves the performance. The attention mechanisms in ViT and its successors [26] assume that tokens are located on a regular grid and therefore could not be used in our networks. To enable the new attention modules in our networks, we developed new equations for attention with relative position embedding. Furthermore, we modified TransDeformer for error estimation, i.e., to estimate the error of a reconstructed geometry. In the following sections, we provide the details of our models. For information not revealed due to the 10-page limit, we refer the reader to the source code.

A. Attention with Relative Position Embedding

To enable the new attention modules in our networks, we developed a new set of equations for attention with relative position embedding. Let X and Y represent two matrices, and each row of a matrix is a token. A token has a unique spatial position. The tokens in X and Y will have different meanings in different attention modules in our networks, which will be explained in other sections. X -to- Y attention refers to using the tokens in X to create queries and using the tokens in Y to create keys and values. When $X = Y$, it is self-attention. The new attention score matrix A is defined as

$$A = \text{softmax} \left(\frac{XW_Q(YW_K)^T R_1 + XW_Q R_2}{\sqrt{d}} \right) \quad (2)$$

W_Q , W_K , W_V are individual linear projections to generate the query, key and value embeddings. We note that in the implementation, the linear projections can be replaced by MLPs. R_1 and R_2 are two matrices encoding relative positions between tokens. d is the embedding dimension of a single attention head.

To better explain Eq.(2), we describe this attention from the perspective of individual tokens. We incorporate the sinusoidal functions to capture the relative position information, which is illustrated as:

$$q_i = \begin{bmatrix} x_i W_Q \odot \cos(p_i W_1 + b_1) \\ x_i W_Q \odot \sin(p_i W_1 + b_1) \\ x_i W_Q \odot \cos(p_i W_2 + b_2) \\ x_i W_Q \odot \sin(p_i W_2 + b_2) \end{bmatrix} \quad (3)$$

$$k_j = \begin{bmatrix} y_j W_K \odot \cos(p_j W_1) \\ y_j W_K \odot \sin(p_j W_1) \\ \cos(p_j W_2) \\ \sin(p_j W_2) \end{bmatrix} \quad (4)$$

In the above equations, q_i denotes a query originated from the token x_i (i.e., the i -th row of X), and k_j denotes a key originated from the token y_j (i.e., the j -th row of Y). p_i is the spatial position of the token x_i . p_j is the spatial position of the token y_j . W_1 , W_2 are trainable weight matrices, and b_1 , b_2 are trainable bias vectors inside the sine and cosine functions to generate different frequency components. \odot denotes the element-wise product of two tensors (vectors or matrices).

Thus, we derive each entry a_{ij} of the attention score matrix A from the scalar dot product of query vector q_i and key vector k_j , which is given by:

$$\begin{aligned} \log(a_{ij}) &\propto \text{sum}(q_i \odot k_j) \\ &= \text{sum}(x_i W_Q \odot y_j W_K \odot \cos((p_i - p_j)W_1 + b_1) \\ &\quad + x_i W_Q \odot \cos((p_i - p_j)W_2 + b_2)) \end{aligned} \quad (5)$$

The final output of an attention layer is the addition of a term similar to Eq.(1) and a term related to the relative positions. The i -th row of the output is calculated by

$$\text{out}_i = \text{Linear}((A_i Y W_V)^T) + \text{Linear} \left(\sum_j a_{ij} (p_i - p_j) \right) \quad (6)$$

where A_i refers to the i -th row of the attention score matrix, Linear refers to a linear layer with trainable weight and bias.

B. UNet-DeformSA

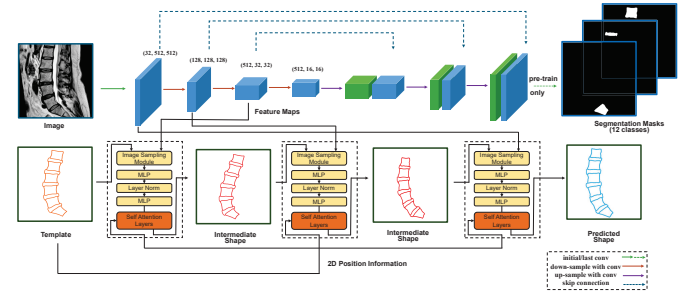


Fig. 2. Structure of UNet-DeformSA. The lumbar spine geometry is reconstructed gradually through three geometry-deformation modules. Each of the modules has shape self-attention layers.

The architecture of UNet-DeformSA is shown in Fig. 2. The UNet backbone facilitates the learning of a hierarchical representation of a lumbar spine MR image (512×512), which consists of 4 encoding layers that output feature maps at 4 spatial resolutions (i.e., 512×512, 128×128, 32×32, and 16×16), and 4 decoding layers with residual connections from the encoding layers. In our experiments, the UNet backbone is pretrained with paired images and segmentation masks, and then the backbone is frozen for feature extraction to serve the other parts of the network. The UNet-DeformSA model has three geometry-deformation modules, and each of which has an image sampling layer and shape self-attention layers. Each geometry-deformation module predicts the displacement vectors at the points of the template shape. In this way, the template shape is deformed gradually by the modules. The shape self-attention layers and the image sampling layer in

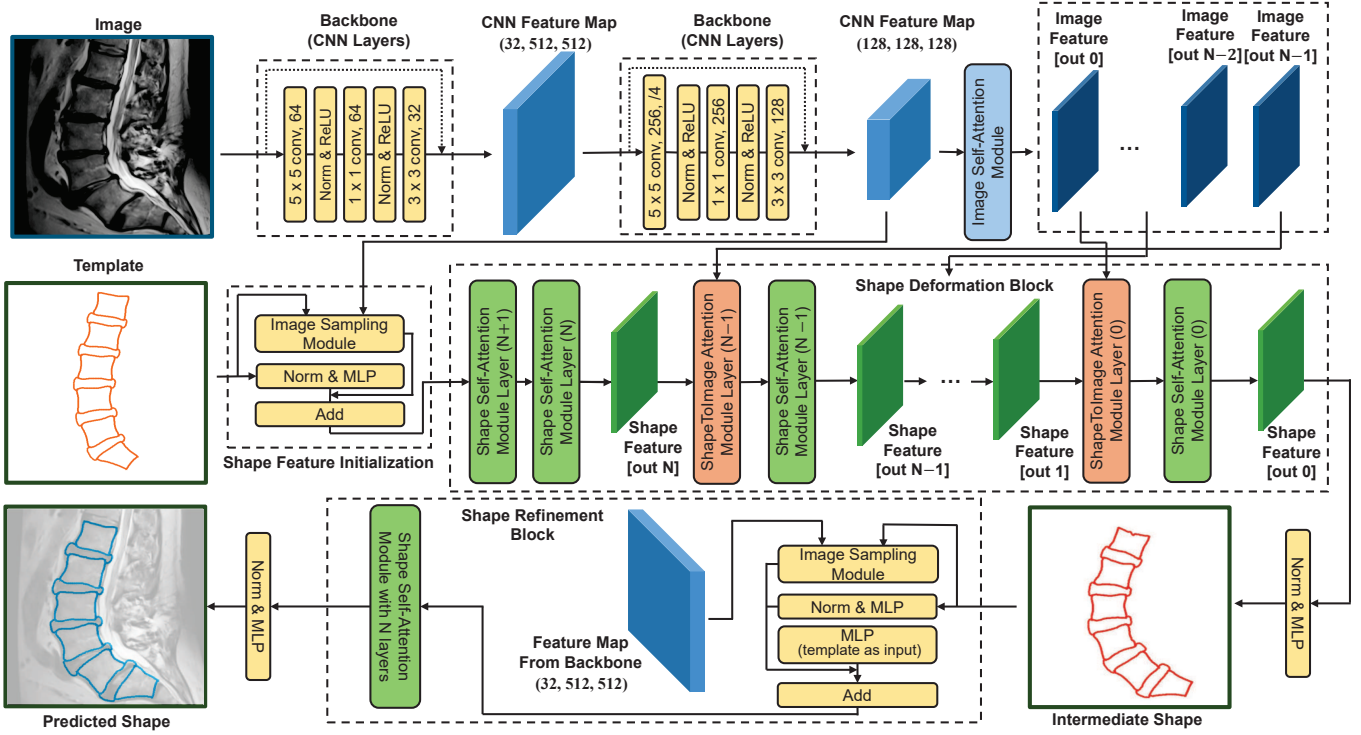


Fig. 3. Structure of TransDeformer.

UNet-DeformSA are the same as those in TransDeformer, and the details are provided in the next section.

C. TransDeformer

The architecture of the TransDeformer model is depicted in Fig. 3. Instead of using a UNet, TransDeformer has two groups of CNN layers serving as two feature extractors at two spatial resolutions (512×512 and 128×128). Given the input template shape, the image sampling module extracts image features at each point of the template shape from the feature maps at the lower resolution. Then, image self-attention, shape self-attention, and shape-to-image attention will be performed to cross-examine and fuse information gathered from individual image patches of the feature maps and points of the template. The final output of the shape self-attention module is used to predict the displacement vectors at the points of the template shape, and then the template is deformed to obtain an “intermediate” shape that is further refined by using the higher resolution feature maps, and this refinement is done through a combination of an image sampling layer and a shape self-attention module that outputs adjustments to the “intermediate” displacement vectors. The refined displacement vectors produce the final output shape. The major components of the TransDeformer model are explained with more details in the following sub-sections.

1) **Image Self-Attention (ISA) Module:** The architecture is depicted in Fig. 4. The ISA module aims to produce the sequential image features with the aggregation of global context from the input CNN feature maps. The CNN feature maps are divided into non-overlapping patches [27], thereby enabling

contextual dependencies across patches as opposed to individual pixels. A patch is a token in the attention mechanism described in Section A. A mesh grid, $G \in \mathbb{R}^{\frac{H}{P} \times \frac{W}{P} \times 2}$ is used for position embedding, where P is the number of patches, H and W are spatial height and width of a patch. Each patch is centered on one of the mesh grid points. The mesh grid coordinates are normalized between -1 and 1. The ISA module has multiple self-attention layers to generate a sequence of feature matrices with increasing long-range associate information. Each row of a feature matrix $Y_i \in \mathbb{R}^{L \times E}$ is a token, where L is the number of patches/tokens and E is the embedding/feature dimension.

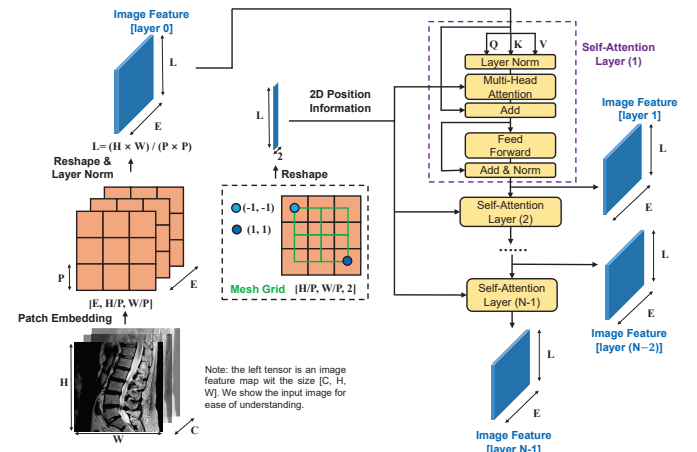


Fig. 4. The overview of image self-attention (ISA) module.

2) *Image Sampling Module*: At each point of the template shape, an image feature vector is extracted by bilinear interpolation in the feature maps and then combined with a position embedding vector. A shape is described not only by a set of points but also by embeddings/features at those points.

3) *Shape Self-Attention (SSA) Module*: The architecture is depicted in Fig. 5. The SSA module aims to learn contextual dependencies across the points of a shape, where individual points are associated with embedding vectors that collectively form the shape feature matrix $X_S \in \mathbb{R}^{N_p \times E}$. N_p is the number of points/tokens of the shape and E is the embedding/feature dimension. A row in the matrix X_S is a token in the attention mechanism described in Section A. For self-attention calculation, the position of a token is defined on the undeformed template with normalized coordinates between -1 and 1. The SSA module has multiple self-attention layers to generate a sequence of feature matrices.

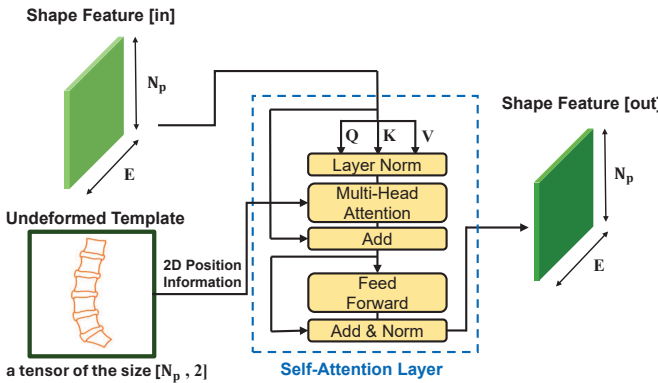


Fig. 5. The overview of the shape self-attention (SSA) module

4) *Shape-to-Image Attention (S2IA) Module*: The architecture is depicted in Fig. 6, serving as a bridge between the ISA and SSA modules. Given Y_I from a layer of the ISA module and X_S from a layer of the SSA module, a new shape feature matrix $\hat{X}_S \in \mathbb{R}^{N_p \times E}$ is generated by the S2IA module and becomes the input to the next shape self-attention layer. In the S2IA module, the position of a token in X_S is defined in the image space to be compatible with the position of a token in Y_I . X_S -to- Y_I attention follows the formula in Section A, and the output of X_S -to- Y_I attention is \hat{X}_S .

In the first shape self-attention layer, each token/point integrates information from its coordinates, neighbor pixels in the image feature maps, and all the other tokens. If the template is initialized close to the true shape of the lumbar spine, then the information at a token could be sufficient for predicting a displacement vector at the token/point. If the template is initialized far away from the true shape, then the displacement vector at a token could not be accurately predicted only by this layer due to insufficient information. Therefore, cross-attention between shape tokens in X_S and image tokens in Y_I is used to gather information from relevant image patches that may be far away from the current template shape, i.e., fostering the long-range dependencies.

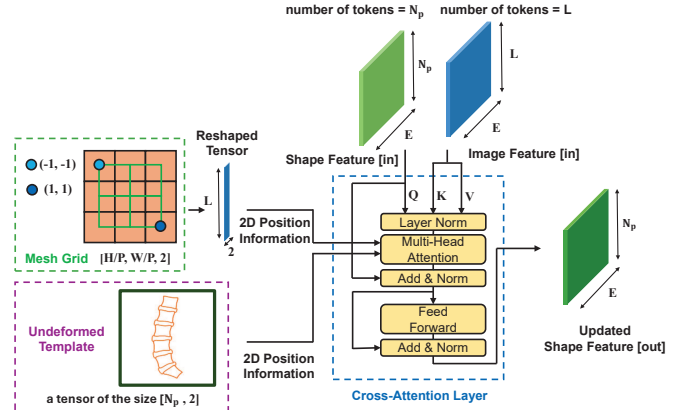


Fig. 6. The overview of the shape-to-image attention (S2IA) module

D. Loss Function, Training and Inference Strategies

To train the UNet-DeformSA model, the loss \mathcal{L} combines a segmentation term \mathcal{L}_{seg} and a geometry term $\mathcal{L}_{\text{geom}}$:

$$\mathcal{L} = \mathcal{L}_{\text{seg}} + \mathcal{L}_{\text{geom}} \quad (7)$$

To train the TransDeformer model, only $\mathcal{L}_{\text{geom}}$ is used because the model does not need image segmentation. \mathcal{L}_{seg} is a blend of Dice loss and area-weighted cross-entropy loss. $\mathcal{L}_{\text{geom}}$ measures the difference between the predicted shape and the ground-truth shape.

Let \bar{M}_i and M_i denote the predicted and the ground truth binary segmentation masks of the i -th class respectively, where $i \in \{0, 1, \dots, n\}$ and class-0 is the background. w_i is a nonnegative scalar inversely proportional to the area of the i -th class, with the constraint $\sum_{i=1}^n w_i = 1$. The segmentation quality term \mathcal{L}_{seg} is formed as:

$$\begin{aligned} \mathcal{L}_{\text{seg}} = & - \sum_{i=1}^n \left[\frac{2 \times \sum(\bar{M}_i \odot M_i)}{\sum \bar{M}_i + \sum M_i} \right] \\ & - \sum_{i=1}^n \left[\sum (w_i M_i \odot \log(\bar{M}_i)) \right] \end{aligned} \quad (8)$$

Also, we proposed a three-stage training strategy to improve spatial accuracy on meshes and robustness to template initialization.

1) *Training Stage 1*: In the first stage, we let the models predict centroids only. Let \hat{C} denote the centroid of a predicted shape \hat{S} (i.e., deformed template). Let C denote the centroid of the corresponding ground truth shape S . Then the loss of geometry quality is formulated as:

$$\mathcal{L}_{\text{geom}}^{(1)}(\hat{S}, S) = \|\hat{C} - C\|_2^2 \quad (9)$$

The template is randomly placed in an image, and then the image and the template are fed to our models during training.

2) *Training Stage 2*: In the second stage, we let the models predict whole shapes. The loss measures the mean squared error (MSE) of the predicted shape \hat{S} , compared to the ground-truth shape S (a flattened array of coordinates of all the points of the shape).

$$\mathcal{L}_{\text{geom}}^{(2)}(\hat{S}, S) = \frac{1}{N_p} \|\hat{S} - S\|_2^2 \quad (10)$$

The template is initialized close to the true shape in an image, and then the image and the template are fed to our models during training.

3) *Training Stage 3*: The loss in the third stage $\mathcal{L}_{\text{geom}}^{(3)}(\hat{S}, S)$ is the same as that in the second stage. The difference is that in the third stage, nonlinear transform is applied to the template before model training. The transformed template is initialized close to the true shape in an image, and then the image and the template are fed to our models during training.

Our models have intermediate shape outputs: UNet-DeformsA has three intermediate shape outputs, and TransDeformer has one intermediate shape output. Our loss function considers not only the final output but also the intermediate shape outputs. The loss of geometry quality at each stage is a combination of the loss terms of the intermediate and final shape outputs.

$$\mathcal{L}_{\text{geom}}^{(t)} = \sum_m \mathcal{L}_{\text{geom}}^{(t)}(\hat{S}^{(m)}, S) \quad (11)$$

where $\hat{S}^{(m)}$ refers to an intermediate shape or the final shape output, and t is stage index.

We used a two-stage inference strategy. In the first stage, the template is initialized in the input image (i.e., template initialization), and the centroid displacement of the template is predicted. In the second stage, the template is re-initialized at the predicted centroid, and then the displacement vectors at individual points of the template are predicted. In experiments, we tested two types of template initialization: random initialization or placing the template at the center of an image.

E. Error Estimation Using a Modified TransDeformer

A model for error estimation takes an image and a shape \hat{S} as the inputs, and predicts the difference between the input shape \hat{S} and the ground-truth shape S of the object in the image. The shape input to the error estimation model could be the output from a shape-reconstruction model (e.g., UNet-DeformSA).

We built such an error estimation model (Fig. 7) by modifying the TransDeformer in the follow steps: (1) take a shape and an image as inputs, (2) remove/bypass the layers that predict the intermediate shape, and (3) output a nonnegative scalar at each point of the input shape. A scalar is an estimation of the distance between a point of the input shape and the corresponding point of the ground-truth shape. During model training, the input shape is random selected from the training dataset and then added with noises, and MSE loss is used.

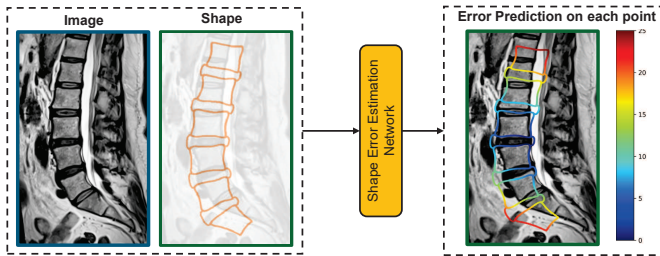


Fig. 7. The overview of the shape error estimation mode (unit: mm).

IV. EXPERIMENTS

A. Dataset

Our dataset [11] consists of de-identified lumbar spine MR images of 100 patients. Three experts annotated and reviewed each mid-sagittal MR image to ensure accuracy and consistency. Each mid-sagittal MR image was manually marked with boundaries and landmarks of the lumbar vertebrae and discs, which is guided by the established protocol [7]. The images are resized to 512×512 . Each image is accompanied with 12 segmentation masks, corresponding to the background, 6 vertebrae (named L1, L2, L3, L4, L5, and S1), and 5 discs (named D1, D2, D3, D4, and D5). We split the entire dataset into 70 training samples, 10 validation samples, and 20 test samples. A special data augmentation method was applied to the original dataset, resulting in 7000 training samples, 250 validation samples, and 2500 test samples. The data augmentation method is described in details in our technical report [11]. Our experiments were conducted on the augmented datasets that are publicly available [11]. Data diversity is illustrated in Fig. 8 by comparing the template with the ground-truth meshes, for which the centroids are aligned.

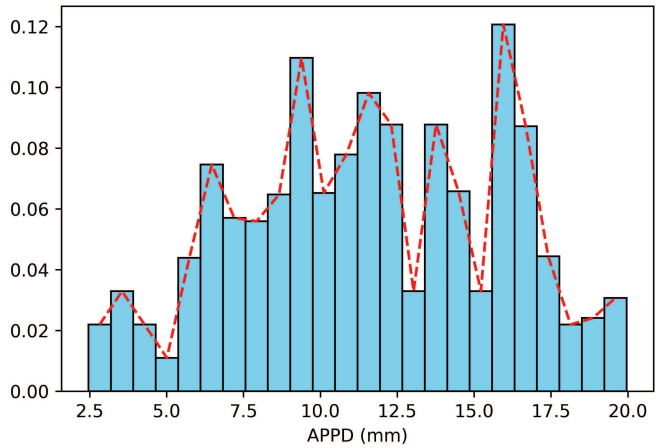


Fig. 8. Distribution of Averaged Point-to-Point Distance (APPD) between the template mesh and the ground truth meshes of the patients in the test set. APPD is defined in Section IV-D.

B. Comparison with Related Approaches

We adapted two related approaches [22], [24] for our application, which were proposed for reconstructing organ geometries by deforming templates through neural networks.

1) *UNet-GCN Model*: This model was originally proposed by Kong et al. [22] for reconstructing human heart geometries from 3D volumetric images. The model has a UNet backbone pretrained for binary segmentation, and the encoder of the UNet is used as the image feature extractor at different scales. Three GCN modules are used to deform a template sequentially by using image features sampled at the points of the template. For our application, we followed the original design as close as possible, and made necessary adjustment by changing the 3D UNet to a 2D UNet to handle 2D sagittal images of lumbar spine. The UNet-GCN model uses GCN

layers to fuse information from neighbour points for displacement prediction. Our UNet-DeformSA model has shape self-attention modules to integrate information from different points that could be far away from each other (i.e., utilizing long-range dependency), which is the key difference from and advantage over the UNet-GCN model.

2) UNet-Disp Model: This model was originally proposed by Pak *et al.* [24] for creating simulation-ready heart valve geometries from 3D CT images. Compared to the UNet-GCN model, the UNet-Disp model also uses a UNet but in a different way: the decoder of the UNet predicts a displacement field that is used to deform a template. For our application, we followed the original design as close as possible, and made necessary adjustment by changing the 3D UNet to a 2D UNet that outputs a 2D displacement field. The UNet-Disp model does not use any attention mechanisms.

3) UNet-MLP Model: This model is a simplification of our UNet-DeformSA by replacing shape self-attention layers with a simple MLP in each geometry-deformation module.

C. Implementation

We used Pytorch ver. 2.0.0 [28] to implement the overall frameworks, and used Pytorch Geometric ver. 2.3.0 [29] to implement GCNs. We used the Adam optimizer with a fixed learning rate of 1e-4 and a batch size of 20. The training of each model completed within 24 hours on a single NVIDIA RTX A6000 with 48GB VRAM.

D. Metrics and Results of Geometry Reconstruction

To measure the accuracy of a reconstructed lumbar object (a vertebra or a disc), we assessed two key metrics: (1) Averaged Point-to-Point Distance (APPD) between a predicted shape and the corresponding ground-truth shape and (2) Dice Similarity Coefficient (Dice), measuring the overlap between areas enclosed by predicted and ground-truth shapes. For each metric, mean, standard deviation (std), the worse case, the 95th or 5th percentile among the test samples are calculated.

The results are reported in Table I and Table II, showing our models outperform the other models. Examples are shown in Fig. 9. Template initialization is done by placing the template at the center of an image.

E. Robustness to Template Initialization

We conducted additional experiments to evaluate a model's robustness with respect to the initial location of the template. The template is placed at the center of an input image, and then a random shift within a circle is applied to the template before feeding it to a model. As the radius of the circle increases, a more robust model has a less reduction in accuracy. The results are reported in Table III, showing that our models are more robust than the other models.

F. Performance of the Shape Error Estimation Model

We used the shape error estimation model to estimate the errors of the outputs from each of the four models for geometry reconstruction, and computed the correlation coefficient between the estimated errors and the true errors. The result is reported in Table IV.

G. Medical Parameter Analysis

1) Medical Parameter Definitions: The template-deformation approach enables consistent definitions and measurements of medical parameters of the lumbar spine. Once a parameter definition is finalized on the template, the parameter of any patient's shape can be straightforwardly measured. Following the previous work [7], we included 15 medical parameters for disc degeneration assessment, which are explained in Fig. 10.

2) Parameter Measurement: To evaluate the accuracy of the measured medical parameters using TransDeformer, we calculated the relative error of each parameter of a patient in the test set. Metrics are mean, standard deviation (std), max, and the 95th percentile of the errors across the patients. Since the reconstructed geometries can be ranked by the errors estimated by the shape error estimation model, these metrics can be evaluated by using $\alpha\%$ of the geometries with the lowest (estimated) errors, where α could be 20, 60, or 100. The results are reported in Table V.

H. Hyperparameter Tuning on Validation Set

For the TransDeformer model, we investigated the effects of patch size P in the ISA module and the number of attention layers in the ISA and SSA modules, and the results on the validation set are reported in Tables VI and VII. Based on the validation performance of the model, patch size of 4 and 2 layers of attention are used in the main experiments.

For the UNet-DeformSA model, we investigated the effect of the number of attention layers in the SSA module, and the results on the validation set are reported in Table VIII. Based on this results, 2 layers of attention are used in the main experiments. For the UNet-GCN model, we evaluated different types of GCN layers and chose ResGatedGraphConv [30] based on the results on the validation set. For the UNet-Disp model, we explored the hyperparameter σ and set it to 1 based on the results on the validation set. The backbone UNet structure is the same for the three models.

V. DISCUSSION

The UNet-MLP model exhibited the lowest accuracy, most likely due to two reasons: (1) CNN layers have limited receptive field sizes and (2) displacement predictions on points are made independently without considering possible correlations. Compared to UNet-MLP, the UNet-GCN model had relatively better accuracy, mostly because the GCN layers predict the displacement of a point by aggregating information from neighbour points on the template because points in a neighborhood are correlated. But, the UNet-GCN model still had much larger errors in some cases, especially in the L1 and D1 regions, which indicates the limitation of GCN. The UNet-Disp model had enhanced accuracy, which is achieved by predicting a displacement field on a regular grid. A major drawback of the UNet-Disp model is that it is not robust to template initialization. As shown by large max and Q95 values in Table I and the examples in Fig. 9, all of the three models generate irregular shapes in some cases.

Our two models, UNet-DeformSA and TransDeformer significantly (p -value $< 1e-6$ using paired t-test) outperformed

TABLE I
PERFORMANCE MEASURED BY APPD (LOWER IS BETTER)

	UNet-MLP				UNet-GCN				UNet-Disp				UNet-DeformSA				TransDeformer			
	mean	std	max	Q95	mean	std	max	Q95	mean	std	max	Q95	mean	std	max	Q95	mean	std	max	Q95
L1	4.152	3.937	21.43	13.09	2.084	3.739	43.27	9.132	1.049	0.897	18.3	1.922	0.608	0.223	2.278	1.039	0.647	0.325	2.937	1.319
D1	2.869	2.877	23.09	8.823	2.151	4.587	47.75	10.62	1.257	1.336	18.39	2.592	0.653	0.217	1.629	1.106	0.692	0.236	1.883	1.17
L2	1.940	1.552	15.21	4.555	1.549	2.846	37.23	6.061	1.196	1.457	16.43	2.305	0.584	0.216	1.392	1.047	0.589	0.211	1.297	0.987
D2	1.667	1.816	20.18	4.000	1.019	1.161	16.67	2.672	1.139	1.117	15.39	2.236	0.681	0.291	3.993	1.164	0.679	0.344	2.884	1.314
L3	1.746	1.504	13.76	4.710	1.207	1.277	9.961	3.503	1.129	1.014	14.59	2.828	0.819	0.452	4.538	1.799	0.824	0.499	3.847	1.801
D3	1.586	0.870	7.584	3.401	1.118	0.789	10.18	2.827	1.072	0.495	8.664	2.023	0.905	0.482	3.191	2.079	0.876	0.427	2.969	1.847
L4	1.692	0.855	10.51	3.327	1.067	0.804	16.25	2.328	0.966	0.420	5.217	1.747	0.864	0.407	5.609	1.535	0.787	0.296	2.455	1.301
D4	2.375	1.789	23.62	5.178	1.359	3.115	26.73	2.701	1.165	0.570	4.697	2.327	0.983	0.543	8.554	1.794	0.987	0.383	3.412	1.723
L5	2.462	2.156	25.42	6.046	1.366	1.480	28.08	2.842	0.940	0.471	5.277	1.860	0.758	0.372	4.022	1.408	0.750	0.292	2.712	1.301
D5	2.554	2.855	34.47	6.436	1.291	1.119	21.38	2.435	1.134	0.524	5.356	2.103	0.759	0.413	11.78	1.27	0.785	0.315	2.406	1.415
S1	2.945	2.935	33.96	7.214	1.324	0.677	7.155	2.507	1.166	0.555	5.126	2.310	0.887	0.801	23.35	1.726	0.818	0.365	3.201	1.511
Whole	2.458	1.272	10.62	5.155	1.435	1.094	10.51	3.385	1.107	0.588	10.5	1.819	0.785	0.259	5.074	1.25	0.769	0.212	1.836	1.198

For a patient, the average of the 11 APPD scores is used as a summary score; mean, std, max, Q95 of the summary scores are reported in the ‘Whole’ row.

TABLE II
PERFORMANCE MEASURED BY DICE (HIGHER IS BETTER)

	UNet-MLP				UNet-GCN				UNet-Disp				UNet-DeformSA				TransDeformer			
	mean	std	min	Q5	mean	std	min	Q5	mean	std	min	Q5	mean	std	min	Q5	mean	std	min	Q5
L1	0.875	0.153	0.022	0.538	0.942	0.114	0.002	0.692	0.968	0.038	0.181	0.945	0.980	0.008	0.936	0.962	0.978	0.010	0.927	0.955
D1	0.846	0.182	0.001	0.409	0.903	0.178	0.000	0.393	0.921	0.133	0.000	0.855	0.964	0.016	0.880	0.930	0.963	0.017	0.870	0.925
L2	0.949	0.070	0.064	0.832	0.956	0.095	0.037	0.824	0.964	0.038	0.516	0.933	0.979	0.010	0.937	0.959	0.979	0.009	0.942	0.962
D2	0.937	0.094	0.024	0.776	0.956	0.049	0.370	0.870	0.934	0.098	0.000	0.844	0.963	0.022	0.684	0.938	0.962	0.024	0.754	0.925
L3	0.952	0.068	0.521	0.830	0.962	0.053	0.615	0.887	0.964	0.031	0.640	0.883	0.969	0.022	0.799	0.923	0.969	0.024	0.840	0.917
D3	0.940	0.054	0.469	0.817	0.949	0.050	0.478	0.826	0.942	0.042	0.235	0.865	0.950	0.035	0.660	0.875	0.951	0.032	0.680	0.880
L4	0.962	0.034	0.383	0.898	0.970	0.037	0.228	0.932	0.970	0.014	0.801	0.945	0.970	0.014	0.835	0.946	0.972	0.011	0.895	0.950
D4	0.918	0.085	0.129	0.768	0.945	0.065	0.025	0.877	0.942	0.030	0.585	0.884	0.952	0.023	0.742	0.911	0.950	0.024	0.762	0.903
L5	0.953	0.059	0.255	0.879	0.966	0.042	0.169	0.938	0.970	0.012	0.849	0.945	0.974	0.011	0.892	0.951	0.975	0.010	0.876	0.956
D5	0.918	0.093	0.155	0.740	0.958	0.040	0.307	0.930	0.943	0.027	0.557	0.900	0.962	0.017	0.673	0.933	0.960	0.019	0.877	0.920
S1	0.928	0.085	0.182	0.791	0.966	0.026	0.506	0.931	0.960	0.021	0.805	0.915	0.968	0.026	0.397	0.935	0.968	0.017	0.884	0.934
Whole	0.925	0.052	0.594	0.813	0.952	0.041	0.623	0.869	0.952	0.033	0.487	0.914	0.967	0.012	0.856	0.942	0.966	0.012	0.881	0.942

For a patient, the average of the 11 dice scores is used as a summary score; mean, std, min, Q5 of the summary scores are reported in the ‘Whole’ row.

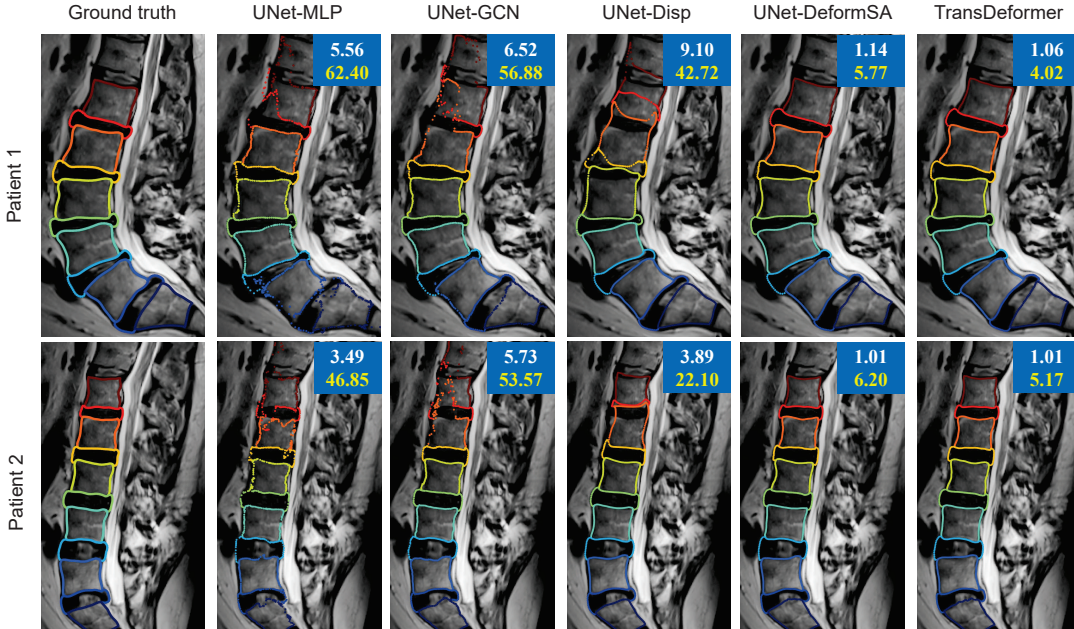


Fig. 9. Outputs of the models on two challenging cases. Different colors indicate different lumbar components. On the upper-right corner, the white number shows the average point-to-point distance error (mm), and the yellow number shows the maximum point-to-point distance error (mm).

the other models as shown by the much lower mean, max, and Q95 values in Table I and the artifact-free geometries in Fig. 9. The novel SSA module in UNet-DeformSA is the key to achieve such high performance by considering long-range dependencies among points of the template. By using two novel attention modules (SIA and S2IA) to utilize long-range dependencies among template points and image

patches, TransDeformer no longer relies on a UNet for feature extraction and performed better than UNet-DeformSA (p-value < 1e-6 using paired t-test).

All of the current ML models for geometry reconstruction, including our models, are data-drive and therefore have no guarantee in output accuracy for an input image. Thus, the geometry output from a ML model has to be checked (and

TABLE III
ROBUSTNESS TO TEMPLATE INITIALIZATION

Radius (pixel)	0	10	20	30	40
UNet-MLP	2.458	2.498	2.760	4.581	8.743
UNet-GCN	1.435	1.472	1.939	3.654	5.860
UNet-Disp	1.107	6.548	13.19	19.52	25.67
UNet-DeformSA	0.784	0.785	0.798	0.879	1.155
TransDeformer	0.769	0.769	0.769	0.769	0.820

Note: APPD (lower is better) is used in the robustness study

TABLE IV
CORRELATION (ρ) BY THE SHAPE ERROR ESTIMATION MODEL

UNet-MLP	UNet-GCN	UNet-Disp	UNet-DeformSA	TransDeformer	
ρ	93.55%	73.55%	95.63%	94.46%	92.54%

modified if necessary) by a human operator to ensure high accuracy for clinical use. The shape error estimation model, which is a modified version of TransDeformer, facilitates this quality control process by ranking the model-reconstructed geometries by the estimated errors. To reduce human negligence, those with larger (estimated) errors will be checked first when the operator is vigilant; and those with smaller (estimated) errors will be checked later when the operator possibly becomes fatigued.

Our study used the mid-sagittal lumbar spine MR images for two major reasons. Firstly, as shown in clinical studies [7], [31], the mid-sagittal image of a patient provides the most useful information for lumbar spine degeneration assessment. Secondly, the slice thickness of a lumbar MR scan in the sagittal direction is often much larger than 5mm, causing difficulties to create accurate 3D ground-truth annotation. Our model could be directly extended to handle 3D images once the sagittal slice thickness becomes acceptably small with the advancement of imaging technology.

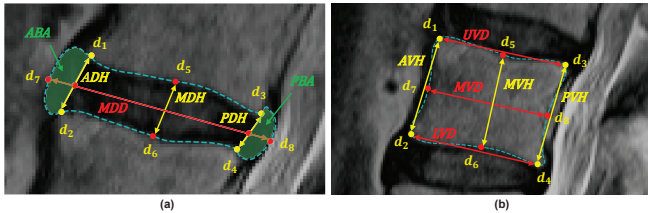


Fig. 10. Definitions of the medical parameters. Corner vertices (d_1 , d_2 , d_3 , and d_4), laying at the intersections between a vertebra and disc, are identified as landmarks. Midpoints (d_5 , d_6 , d_7 , and d_8) on edges are also identified. For vertebrae, we introduce three main parameters, including upper, lower and middle vertebra diameters (UVD, LVD, MVD). Additionally, we measure the height of anterior, posterior and middle vertebra (AVH, PVH, MVH) as well as the mean vertebra height (VHMean), a ratio of the vertebra's area to its diameter, to comprehensively depict the vertebra in cause of its abrasion. Similar to vertebrae, we introduce three main parameters including anterior, posterior and middle disc heights (ADH, PHD, MDH) to measure disc dimensions. The middle diameter of a disc (MDD) is defined as the line extending from the midpoints of landmarks and intersecting with the disc's left and right edges. The mean disc height (DHMean) is calculated as the ratio of the disc's area to this diameter. Moreover, relative anterior and posterior disc bulging areas (rABA, rPBA), ratios of the bulging areas to the averaged disc area, are introduced as critical metrics in evaluating disc degeneration.

VI. CONCLUSION

We proposed two novel attention-based neural networks, UNet-DeformSA and TransDeformer, to automatically reconstruct lumbar spine geometries with mesh correspondence from 2D MR images. The reconstructed geometries are highly accurate and free of artifacts. In addition, we proposed a shape error estimation network based on TransDeformer, which facilitates quality control. Thus, we have provided a complete solution for fast and accurate measurement of the key medical parameters of lumbar spine components from MR images.

REFERENCES

- [1] J.S. Duncan and N. Ayache. Medical image analysis: progress over two decades and the challenges ahead. *IEEE Transactions on Pattern Analysis and Machine Intelligence*, 22(1):85–106, 2000.
- [2] Geert Litjens, Thijs Kooi, Babak Ehteshami Bejnordi, Arnaud Arindra Adiyoso Setio, Francesco Ciompi, Mohsen Ghafoorian, Jeroen A.W.M. van der Laak, Bram van Ginneken, and Clara I. Sánchez. A survey on deep learning in medical image analysis. *Medical Image Analysis*, 42:60–88, 2017.
- [3] Sertac Kirnaz, Charisse Capadona, Taylor Wong, Jacob L Goldberg, Branden Medary, Fabian Sommer, Lynn B McGrath Jr, and Roger Härtl. Fundamentals of intervertebral disc degeneration. *World Neurosurgery*, 157:264–273, 2022.
- [4] Aimin Wu, Lyn March, Xuanqi Zheng, Jinfeng Huang, Xiangyang Wang, Jie Zhao, Fiona M Blyth, Emma Smith, Rachelle Buchbinder, and Damian Hoy. Global low back pain prevalence and years lived with disability from 1990 to 2017: estimates from the global burden of disease study 2017. *Annals of translational medicine*, 8(6), 2020.
- [5] Worku Abie Liyew. Clinical presentations of lumbar disc degeneration and lumbosacral nerve lesions. *International journal of rheumatology*, 2020, 2020.
- [6] Christian WA Pfirrmann, Alexander Metzdorf, Marco Zanetti, Juerg Hodler, and Norbert Boos. Magnetic resonance classification of lumbar intervertebral disc degeneration. *spine*, 26(17):1873–1878, 2001.
- [7] Xiaojian Hu, Mingjian Chen, Jianjiang Pan, Liang Liang, and Yue Wang. Is it appropriate to measure age-related lumbar disc degeneration on the mid-sagittal mr image? a quantitative image study. *European Spine Journal*, 27:1073–1081, 2018.
- [8] Yangyang Cui, Jia Zhu, Zhili Duan, Zhenhua Liao, Song Wang, and Weiqiang Liu. Artificial intelligence in spinal imaging: current status and future directions. *International journal of environmental research and public health*, 19(18):11708, 2022.
- [9] Tapio Videman, Laura E Gibbons, and Michele C Battié. Age-and pathology-specific measures of disc degeneration. *Spine*, 33(25):2781–2788, 2008.
- [10] J Richard Landis and Gary G Koch. The measurement of observer agreement for categorical data. *biometrics*, pages 159–174, 1977.
- [11] Jiasong chen, Linchen Qian, Linhai Ma, Timur Urakov, Weiyong Gu, and Liang Liang. Evaluation of deep neural network models for instance segmentation of lumbar spine mri. *bioRxiv:2024.04.02.587810*, 2024.
- [12] Zongwei Zhou, Md Mahfuzur Rahman Siddiquee, Nima Tajbakhsh, and Jianming Liang. Unet++: A nested u-net architecture for medical image segmentation. In *Deep Learning in Medical Image Analysis and Multimodal Learning for Clinical Decision Support: 4th International Workshop, DLMIA 2018, and 8th International Workshop, ML-CDS 2018, Held in Conjunction with MICCAI 2018, Granada, Spain, September 20, 2018, Proceedings 4*, pages 3–11. Springer, 2018.
- [13] Jieneng Chen, Yongyi Lu, Qihang Yu, Xiangde Luo, Ehsan Adeli, Yan Wang, Le Lu, Alan L Yuille, and Yuyin Zhou. Transunet: Transformers make strong encoders for medical image segmentation. *arXiv preprint arXiv:2102.04306*, 2021.
- [14] Hu Cao, Yueyue Wang, Joy Chen, Dongsheng Jiang, Xiaopeng Zhang, Qi Tian, and Manning Wang. Swin-unet: Unet-like pure transformer for medical image segmentation. In *European conference on computer vision*, pages 205–218. Springer, 2022.
- [15] Hua-Dong Zheng, Yue-Li Sun, De-Wei Kong, Meng-Chen Yin, Jiang Chen, Yong-Peng Lin, Xue-Feng Ma, Hong-Shen Wang, Guang-Jie Yuan, Min Yao, et al. Deep learning-based high-accuracy quantitation for lumbar intervertebral disc degeneration from mri. *Nature communications*, 13(1):841, 2022.

TABLE V
RELATIVE ERROR OF MEDICAL PARAMETER MEASUREMENT (LOWER IS BETTER)

$\alpha\%$	100%				60%				20%			
	mean	std	max	Q95	mean	std	max	Q95	mean	std	max	Q95
UVD	1.75%	0.83%	6.44%	3.61%	1.49%	0.52%	4.24%	2.49%	1.45%	0.50%	3.67%	2.35%
LVD	2.23%	0.91%	6.82%	3.89%	1.95%	0.74%	5.35%	3.28%	1.77%	0.65%	4.02%	2.96%
MVD	2.44%	1.34%	7.65%	5.09%	2.02%	1.04%	7.08%	4.02%	1.76%	0.80%	4.31%	3.61%
AVH	2.10%	1.08%	8.87%	4.15%	1.80%	0.85%	6.67%	3.26%	1.56%	0.66%	3.84%	2.78%
PVH	2.24%	0.90%	6.64%	3.93%	1.98%	0.74%	6.08%	3.32%	1.89%	0.71%	4.57%	3.20%
MVH	2.06%	1.33%	12.89%	4.58%	1.59%	0.81%	5.33%	3.14%	1.33%	0.68%	3.78%	2.72%
VH mean	1.87%	1.08%	8.91%	4.08%	1.43%	0.55%	3.52%	2.42%	1.26%	0.47%	2.76%	2.12%
XY	1.21%	0.72%	7.37%	2.55%	1.04%	0.52%	3.34%	2.02%	0.98%	0.53%	2.96%	1.99%
ADH	4.48%	2.20%	15.55%	8.95%	3.68%	1.58%	11.49%	6.59%	3.10%	1.21%	6.99%	5.46%
PDH	7.23%	3.68%	28.22%	14.13%	6.42%	2.98%	17.27%	11.94%	6.43%	2.97%	16.42%	11.59%
MDH	4.73%	2.82%	23.24%	10.21%	4.05%	2.17%	12.35%	8.29%	3.67%	2.00%	11.29%	7.66%
DH mean	3.48%	1.94%	16.16%	6.88%	2.84%	1.34%	8.14%	5.36%	2.60%	1.18%	6.37%	4.84%
ABA	1.81%	0.86%	7.80%	3.42%	1.58%	0.58%	3.63%	2.65%	1.43%	0.48%	3.24%	2.22%
PBA	0.99%	0.44%	2.98%	1.83%	0.95%	0.42%	2.85%	1.75%	0.90%	0.37%	2.44%	1.57%
disc area	3.59%	1.79%	12.69%	6.92%	2.94%	1.21%	7.15%	4.99%	2.78%	1.08%	6.08%	4.77%

TABLE VI
HYPERPARAMETER TUNING ON PATCH SIZE

patch size	APPD (mm)			
	mean	std	max	Q95
2	0.574	0.127	1.001	0.795
4	0.569	0.121	0.951	0.787
8	0.612	0.170	1.283	0.896
16	0.605	0.154	1.052	0.886

Note: TransDeformer results (lower is better)

TABLE VIII
HYPERPARAMETER TUNING ON THE NUMBER OF ATTENTION LAYERS

N	APPD (mm)			
	mean	std	max	Q95
2	0.569	0.121	0.951	0.787
4	0.581	0.137	0.981	0.851
6	0.593	0.150	1.017	0.851
8	0.562	0.140	1.023	0.821

Note: UNet-DeformSA results (lower is better)

TABLE VII

HYPERPARAMETER TUNING ON THE NUMBER OF ATTENTION LAYERS

N	APPD (mm)			
	mean	std	max	Q95
2	0.569	0.121	0.951	0.787
4	0.581	0.137	0.981	0.851
6	0.593	0.150	1.017	0.851
8	0.562	0.140	1.023	0.821

Note: TransDeformer results (lower is better)

- [16] Lawrence H Staib and James S Duncan. Model-based deformable surface finding for medical images. *IEEE transactions on medical imaging*, 15(5):720–731, 1996.
- [17] Timothy F. Cootes, Gareth J. Edwards, and Christopher J. Taylor. Active appearance models. *IEEE Transactions on pattern analysis and machine intelligence*, 23(6):681–685, 2001.
- [18] Yefeng Zheng, Adrian Barbu, Bogdan Georgescu, Michael Scheuering, and Dorin Comaniciu. Four-chamber heart modeling and automatic segmentation for 3-d cardiac ct volumes using marginal space learning and steerable features. *IEEE transactions on medical imaging*, 27(11):1668–1681, 2008.
- [19] Liang Liang, Fanwei Kong, Caitlin Martin, Thuy Pham, Qian Wang, James Duncan, and Wei Sun. Machine learning-based 3-d geometry reconstruction and modeling of aortic valve deformation using 3-d computed tomography images. *International journal for numerical methods in biomedical engineering*, 33(5):e2827, 2017.
- [20] Zonghan Wu, Shirui Pan, Fengwen Chen, Guodong Long, Chengqi Zhang, and Philip S. Yu. A comprehensive survey on graph neural networks. *IEEE Transactions on Neural Networks and Learning Systems*, 32(1):4–24, 2021.
- [21] Udaranga Wickramasinghe, Edoardo Remelli, Graham Knott, and Pascal Fua. Voxel2mesh: 3d mesh model generation from volumetric data. In *Medical Image Computing and Computer Assisted Intervention–MICCAI 2020: 23rd International Conference, Lima, Peru, October 4–8, 2020, Proceedings, Part IV 23*, pages 299–308. Springer, 2020.

- [22] Fanwei Kong, Nathan Wilson, and Shawn Shadden. A deep-learning approach for direct whole-heart mesh reconstruction. *Medical image analysis*, 74:102222, 2021.
- [23] Adrian V Dalca, Guha Balakrishnan, John Guttag, and Mert R Sabuncu. Unsupervised learning of probabilistic diffeomorphic registration for images and surfaces. *Medical image analysis*, 57:226–236, 2019.
- [24] Daniel H Pak, Minliang Liu, Theodore Kim, Liang Liang, Andres Caballero, John Onofrey, Shawn S Ahn, Yilin Xu, Raymond McKay, Wei Sun, et al. Patient-specific heart geometry modeling for solid biomechanics using deep learning. *IEEE transactions on medical imaging*, 2023.
- [25] Fahad Shamshad, Salman Khan, Syed Waqas Zamir, Muhammad Haris Khan, Munawar Hayat, Fahad Shahbaz Khan, and Huazhu Fu. Transformers in medical imaging: A survey. *Medical Image Analysis*, 88:102802, 2023.
- [26] Kai Han, Yunhe Wang, Hanting Chen, Xinghao Chen, Jianyuan Guo, Zhenhua Liu, Yehui Tang, An Xiao, Chunjing Xu, Yixing Xu, et al. A survey on vision transformer. *IEEE transactions on pattern analysis and machine intelligence*, 45(1):87–110, 2022.
- [27] Alexey Dosovitskiy, Lucas Beyer, Alexander Kolesnikov, Dirk Weissenborn, Xiaohua Zhai, Thomas Unterthiner, Mostafa Dehghani, Matthias Minderer, Georg Heigold, Sylvain Gelly, et al. An image is worth 16x16 words: Transformers for image recognition at scale. *arXiv preprint arXiv:2010.11929*, 2020.
- [28] Adam Paszke, Sam Gross, Francisco Massa, Adam Lerer, James Bradbury, Gregory Chanan, Trevor Killeen, Zeming Lin, Natalia Gimelshein, Luca Antiga, et al. Pytorch: An imperative style, high-performance deep learning library. *Advances in neural information processing systems*, 32, 2019.
- [29] Matthias Fey and Jan Eric Lenssen. Fast graph representation learning with pytorch geometric. *arXiv* 2019. *arXiv preprint arXiv:1903.02428*, 1903.
- [30] Xavier Bresson and Thomas Laurent. Residual gated graph convnets. *arXiv preprint arXiv:1711.07553*, 2017.
- [31] Shota Tamagawa, Daisuke Sakai, Hidetoshi Nojiri, Masato Sato, Muneaki Ishijima, and Masahiko Watanabe. Imaging evaluation of intervertebral disc degeneration and painful discs—advances and challenges in quantitative mri. *Diagnostics*, 12(3), 2022.